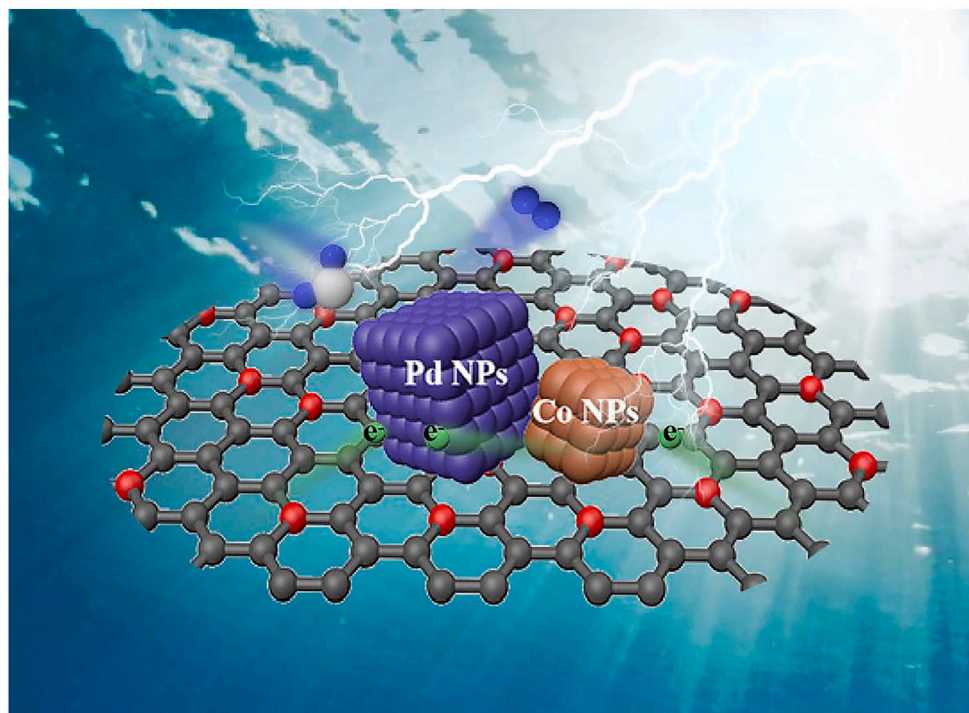


Article

Mechanism insight into the N-C polar bond and Pd-Co heterojunction for improved hydrogen evolution activity



Chenliang Zhou,
Shaoyuan Shi,
Xingyu Zhang,
Yuting Sun, Guan
Peng, Wenjing
Yuan

wjyuan@gia.cas.cn

Highlights

N-C polar bond and Pd-Co heterojunction are constructed

A novel electron-transfer path is found

This study opens a window for the design of heterojunction for HER

Zhou et al., iScience 27, 109620
May 17, 2024 © 2024 The
Authors. Published by Elsevier
Inc.
[https://doi.org/10.1016/
j.isci.2024.109620](https://doi.org/10.1016/j.isci.2024.109620)

Article

Mechanism insight into the N-C polar bond and Pd-Co heterojunction for improved hydrogen evolution activity

Chenliang Zhou,^{1,2} Shaoyuan Shi,^{1,2,3,4} Xingyu Zhang,^{1,2} Yuting Sun,^{1,2} Guan Peng,¹ and Wenjing Yuan^{1,2,3,5,*}

SUMMARY

Constructing platinum-like materials with excellent catalytic activity and low cost has great significance for hydrogen evolution reaction (HER) during electrolysis of water. Herein, palladium nanoparticles (NPs) deposition on the surface of Co NPs using nitrogen-doped carbon (NC) as substrate, denoted as N-ZIFC/CoPd-30, are manufactured and served as HER electrocatalysts. Characterization results and density functional theory calculations validate that Pd-Co heterojunctions with NC acting as “electron donors” promote the Pd species transiting to the electron-rich state based on an efficient electron transfer mechanism, namely the N-C polar bonds induced strong metal-support interaction effect. The electron-rich Pd sites are beneficial to HER. Satisfactorily, N-ZIFC/CoPd-30 have only low overpotentials of 16, 162, and 13 mV@-10 mA cm⁻² with the small Tafel slopes of 98 mV/decade, 126 mV/decade, and 72 mV/decade in pH of 13, 7, and 0, respectively. The success in fabricating N-ZIFC/CoPd opens a promising path to constructing other platinum-like electrocatalysts with high HER activity.

INTRODUCTION

Human society expansion has resulted in an ongoing scarcity of conventional fossil energy and a series of ecological issues nowadays. Developing a clean and renewable energy is essential to addressing these problems.^{1–3} Among numerous clean energies, H₂ has received wide attention in recent years due to its characteristics of high energy density (142.5 kJ/g) and zero pollutants.^{4–7} However, using steam reforming or coal gasification to produce H₂ will lead to unavoidable energy consumption and environmental pollution issues.^{8,9} Water splitting driven by electric power is a clean and highly effective method to produce green H₂, and hydrogen evolution reaction (HER) is an important half-reaction during the process of electrolyzing water.^{10–12} At present, proton exchange membrane electrolyzes,¹³ alkaline electrolyzes,¹⁴ and microbial electrolyzes¹⁵ are employed for producing high-purity H₂ in acidic, alkaline, and neutral media, respectively. Therefore, it is crucial to develop a high-activity catalyst in a broad pH range to ensure effective H₂ preparation. Though platinum (Pt)-based materials are the benchmarking HER electrocatalyst for H₂ production,^{16–18} its high expenses and scarcity hinder their large-scale application.¹⁹ Meanwhile, the catalytic activities of Pt-based materials in neutral and alkaline media are inferior.²⁰ Hence, it is urgent to design and produce Pt-free HER catalysts with outstanding performance in a wide pH range as well as an acceptable cost.

The electronic structures and chemical properties of palladium (Pd) with a greater reserve (2–3 times) are similar to those of Pt²¹; however, its electrochemical performance is still scarcely equal to that of Pt-based catalyst because the adsorption of H_{ads} on the surface of Pd is too strong due to its higher d-band center.^{22,23} Considerable efforts have been invested in the regulation of Pd electronic structure to strengthen its catalytic properties, involving alloying Pd with Fe,²⁴ Co,²⁵ Cu,²⁶ or other noble metal elements Pt,²⁷ Ir,²⁸ Rh,²⁹ Ru,³⁰ building core-shell heterostructure,³¹ selecting ideal materials to support Pd, and so on. Among these strategies, choosing optimal materials, including oxide,^{32–34} carbide,³⁵ sulfide,^{36,37} selenide,³⁸ carbon materials,³⁹ etc, to support Pd has been demonstrated to be a promising, straightforward, and efficacious method. In carbon materials, nitrogen-doped carbon (NC) can enhance the interaction between substrate and metal due to the formation of C-N polar bond that activates the inert carbon π electrons, improving the catalytic performance. For example, Liu et al. used nitrogen-doped graphene (NG) to support Pd nanoparticles (NPs) and denoted them as Pd/NG. The overpotential of Pd/NG at 10 mA cm⁻² is 199 mV, smaller than that of Pd/G (218 mV).⁴⁰ Meanwhile, transition metal (TM = Fe, Co, Ni) embedded in NC (TM@NC) is always regarded as a more ideal carrier, because TM in TM@NC can further increase the interaction between the support and metal as well as change Pd d-band filling levels.⁴¹ Specially, Co@NC, derived from the pyrolytic process of Co-based metal-organic framework (MOF) materials, has drawn wide attention due to its abundant pore structure and good electroconductibility.^{42–44} Though Co possess well intrinsic electrocatalytic

¹Ganjiang Innovation Academy, Chinese Academy of Sciences, Ganzhou 341119, People's Republic of China²School of Rare Earths, University of Science and Technology of China, Hefei 230026, People's Republic of China³Jiangxi Province Key Laboratory of Cleaner Production of Rare Earths, Ganzhou 341119, People's Republic of China⁴Institute of Process Engineering, Chinese Academy of Sciences, Beijing 100190, People's Republic of China⁵Lead contact

*Correspondence: wjyuan@gia.cas.cn

<https://doi.org/10.1016/j.isci.2024.109620>

activity due to its half-filled 3d orbitals, the HER activity of Co@NC is far from fulfilling the requirements of practical applications. However, its catalytic performance can apparently be enhanced after loading Pd due to the interaction between Co and Pd. For instance, the Co@Pd NPs encapsulated in NC were studied by Yang et al., with ZIF-67 as the raw material.⁴⁵ The prepared HER catalyst possesses an overpotential of 98 mV@10 mA cm⁻² and a small Tafel slope of 55.7 mV/decade. Liu et al. constructed Pd_{0.12}/Co@NC catalysts with Co-BTC as the precursor.⁴⁶ The optimized electrocatalyst exhibits an excellent HER activity with an overpotential of 54 mV@10 mA cm⁻² and a Tafel slope of 42 mV/decade in 0.5 M H₂SO₄. However, there are few reports about Pd NPs anchored in Co@NC derived from Co-MOF exhibiting outstanding HER activity in a broad pH range. Meanwhile, the detailed explanation of the interaction between Co@NC and Pd NPs, as well as the origin of the distinguished HER activity of Pd NPs over a wide pH range, remains to be clarified.

In this work, Pd NPs supported on Co@NC derived from the pyrolysis of ZIF-67 (denoted as N-ZIFC/CoPd-30) was fabricated. According to the characterization results and density functional theory (DFT) calculations, the mechanism of Co@NC enhancing the HER activity of Pd has the following two aspects. On the one hand, Co can form a Co-Pd heterojunction with Pd and act as "electron contributors." On the other hand, N atoms activate inert carbon π electrons, and promote the formation of the C-N polar bond, acting as an electron-transfer path between Pd NPs and substrate, further inducing the generation of the electron-rich state Pd. Thus, the optimized electrocatalyst performs satisfactorily HER activity with an overpotential of 16, 162, and 13 mV@-10 mA cm⁻² at pH of 13, 7, and 0, respectively. In our opinion, this study opens a window for the design of HER electrocatalysts with excellent activity over a broad pH range.

RESULTS AND DISCUSSION

Electrocatalyst characterization

The process of Pd NPs deposition on the surface of ZIF-derived carbon materials (N-ZIFC/CoPd) is illustrated in Figure 1A. Specifically, the as-prepared ZIF-67 was firstly calcinated in Ar atmosphere and obtained N-ZIFC/Co. Secondly, N-ZIFC/Co was mixed with PdCl₂ solution at room temperature, and dried in the oven at 80°C for 3 days. Finally, after calcining in 5 vol % H₂ (Ar balance), the resultant N-ZIFC/CoPd was obtained. The morphology, microstructure, and element composition of as-synthesized samples were the first to be studied. As shown in Figure S1A (see the supplemental information), the ZIF-67 with uniform size distribution and smooth surface is obviously observed. However, the rough shell is formed on the surface of N-ZIFC (Figure S1B, see the supplemental information), which is likely because of the formation of volatile gas, and leads to the generation of rough structure. As shown in Figures 1B and S1C (see the supplemental information), SEM images of N-ZIFC/CoPd-30 and N-ZIFC/Co have a similar morphological structure. The regular morphology is well maintained. It is further confirmed by transmission electron microscope (TEM) and STEM images in Figures 1C and 1E. The HRTEM image of N-ZIFC/CoPd-30 in Figure S2 (see the supplemental information) displays the lattice fringes with a lattice spacing of 0.217 nm corresponding to the (100) plane of hexagonal Co, indicating that the Co element in ZIF-67 has been reduced to metallic Co by high-temperature heating. In Figure 1D, besides the lattice fringes of Co NPs, clear lattice fringes with a lattice spacing of 0.225 nm were also observed, which belong to the Pd (111) plane.^{47,48} According to the HRTEM results, Pd was successfully modified on the surface of Co NPs, forming a Pd-Co heterojunction, which is favorable to fully integrating the benefits of Co and Pd, and improving the interaction between N-ZIFC/Co and Pd. The STEM and element mapping of N-ZIFC/CoPd-30 were performed as displayed in Figures 1E–1J, the C, O, N, Co, and Pd elements are clearly observed, confirming that the typical sample is composed of N-ZIFC, Co NPs, and Pd NPs. Additionally, the contents of Co and Pd in N-ZIFC/CoPd-30 are 24.95 and 10.61 wt % according to the result of ICP analysis (Table S1, see the supplemental information). Besides, the contents of Pd in N-ZIFC/CoPd-1 and N-ZIFC/CoPd-10 are 0.64 and 3.23 wt % (Table S2, see the supplemental information). These aforementioned results prove that Pd is successfully deposited on the surface of N-ZIFC/Co.

XRD was further performed to verify the crystal structure of electrocatalysts. Figure S3 (see the supplemental information) displays the XRD patterns of ZIF-67, matching well with the reported literature.⁴⁹ As shown in Figure 2A, XRD results confirm that N-ZIFC/Co, N-ZIFC/CoPd-1, N-ZIFC/CoPd-10, and N-ZIFC/CoPd-30 samples do not exhibit the characteristic peaks of ZIF-67, revealing that the ZIF-67 is completely carbonized and converted to porous carbon, which can be proved by the peak located at around 26° associated with the diffraction of (002) plane of graphite carbon. Meanwhile, there are two kinds of Co species in N-ZIFC/CoPd-1, N-ZIFC/CoPd-10 and N-ZIFC/CoPd-30: the diffraction peaks located at about 44°, 52°, and 76° are assigned to the cubic Co (111), (200), and (220) planes (PDF#15-0806), and the three diffraction peaks located at about 42°, 45°, and 48° belong to the hexagonal Co (100), (002), and (101) planes (PDF#05-0727). Besides, the typical sample exhibits some other peaks centered at around 40°, 47°, and 68°, which belong to the Pd (111), (200), and (220) planes (PDF#65-2867). The aforementioned results suggest that ZIF-67 can be completely carbonized with Co^{x+} in ZIF-67 being transformed to Co⁰ in high-temperature calcination process, and the Pd NPs are successfully deposited on the surface of N-ZIFC/Co.

Nitrogen adsorption-desorption measurements were conducted to verify the surface areas and porosity of the samples. From Figure S4 (see the supplemental information), the N-ZIFC and N-ZIFC/CoPd-30 samples possess a similar pore size distribution with a pore size of approximately 3–4 nm. In Figure 2B, the BET surface area of N-ZIFC/CoPd-30 and N-ZIFC is 233 and 259 m² g⁻¹ in turn. The high BET surface area and abundant porosity of N-ZIFC/CoPd-30 are beneficial to expose the active sites as much as possible, mass transfer, and bubble diffusion during the HER process.⁵⁰

Furthermore, X-ray photoelectron spectroscopy (XPS) was also conducted to verify the element types and valence states of samples. In Figure 2C, there are five peaks of N-ZIFC/CoPd-30 located at around 782, 340, 285, 400, and 534 eV, referring to Co 2p, Pd 3d, C 1s, N 1s, and O 1s, which match the results of element mapping images in Figures 1F–1J. Besides, the intensity of Pd 3d of N-ZIFC/CoPd increases with the Pd content increment, fitting with the experimental process, as displayed in Figure S5 (see the supplemental information). The C 1s spectra (Figure S6, see the supplemental information) can be divided into five distinct peaks of C-C (284.78 eV), C-O (285.67 eV), C-N

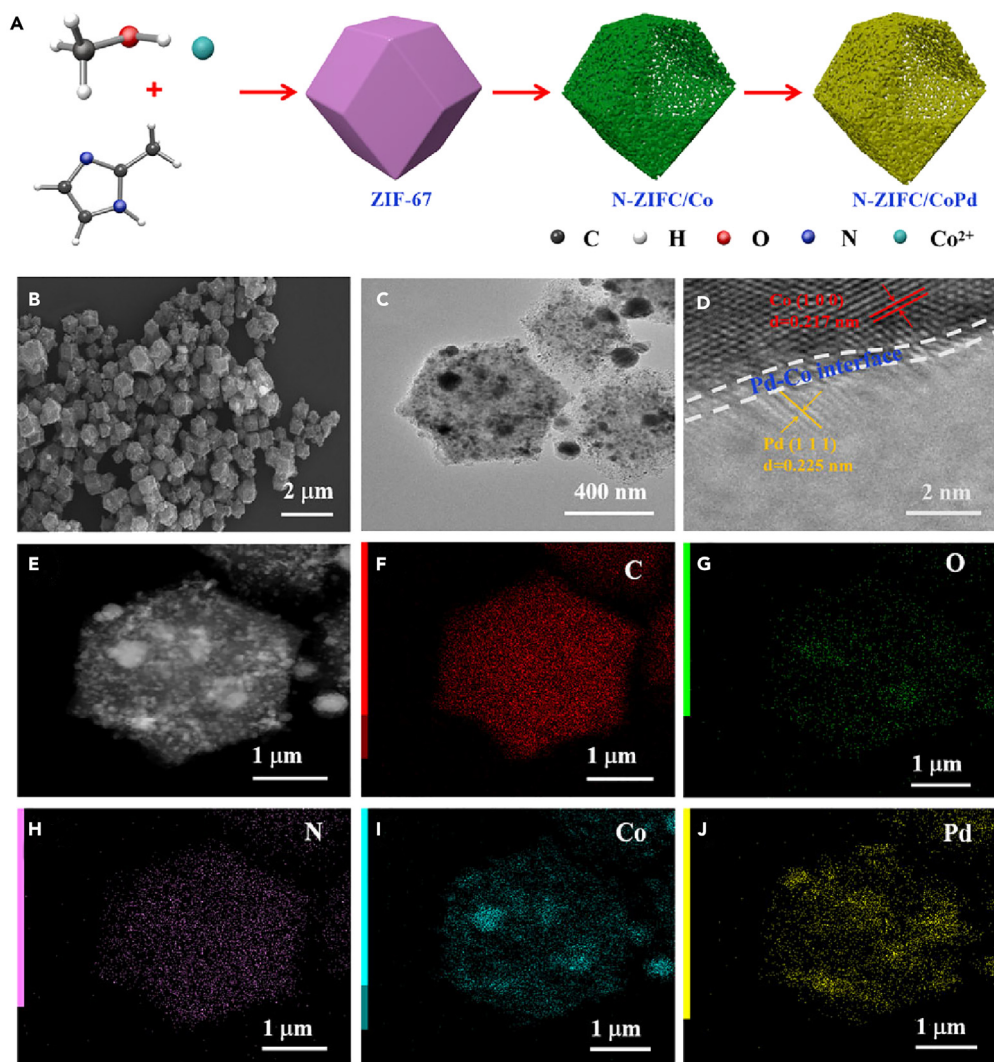


Figure 1. Schematic illustration for the preparation of N-ZIF/CoPd and morphology characterizations of N-ZIF/CoPd-30

(A) Schematic illustration for the construction of N-ZIF/CoPd samples.

(B) SEM.

(C) TEM.

(D) HRTEM.

(E) STEM.

(F–J) Element mapping images of N-ZIF/CoPd-30.

(286.72 eV), C=O (288.10 eV), and Pi-Pi (290.43 eV).⁵¹ It is obvious that the five peaks in the C 1s spectrum of three samples have little difference, suggesting that a negligible interaction between the C atom and Pd atom. From the N 1s spectra of N-ZIF/CoPd-30 (Figure 2D), the four peaks located at about 403.5, 401.32, 400.22, and 398.7 eV, in accordance with oxidized N, graphitic N, pyrrolic N, and pyridinic N in turn, further revealing the doping of nitrogen into carbon.⁵² Compared with N-ZIFC and N-ZIFC/Co, the N 1s peaks move to higher binding energy after the loaded of Pd NPs. This result indicates that there are obvious electron transfers between Pd and N.⁵³ The electrons transferring from NC to Pd regulate the HER process over a broad pH range, positively altering the HER activity of the catalysts. Besides, the HER activity of N-ZIFC/CoPd enhances with the increase in N content according to the XPS result (Table S3, see supplemental information), further proving the key role of N doping. In Figure 2E, there are two double peaks in the Pd 3d high resolution spectrum of N-ZIFC/CoPd-30, which are attributed to metallic Pd (Pd⁰) and oxidized Pd (Pd²⁺). The presence of metallic Pd is in agreement with previous XRD and TEM results. The Pd²⁺ species may originate from the inevitable surface oxidation when exposed to the air atmosphere. Besides, the peak located at 338.2 eV is assigned to Pd-N species, reflecting that Pd NPs anchor on the surface of NC through N atoms.⁵⁴ In Figure 2F, the Co 2p spectra of N-ZIFC/CoPd-30 can be divided into five peaks, Co⁰ (778.5 eV), Co²⁺ (779.2 eV), Co³⁺ (780.9 eV), Co-N (782.3 eV), and satellite peak (786.1 eV).⁵⁵ Moreover, compared to N-ZIFC, the position of Co 2p_{3/2} in N-ZIFC/CoPd-30 shifted around 0.3 eV toward the higher energy direction,

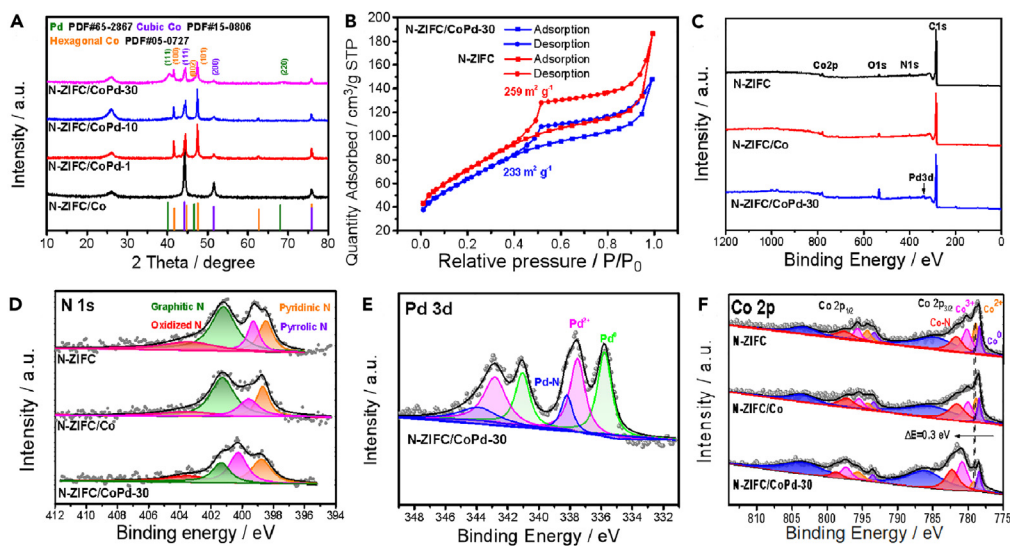


Figure 2. Structure and composition analysis of the materials

- (A) XRD patterns of N-ZIF/Co, N-ZIF/CoPd-1, N-ZIF/CoPd-10, and N-ZIF/CoPd-30.
 (B) Nitrogen adsorption-desorption isotherms of N-ZIF and N-ZIF/CoPd-30.
 (C) XPS survey spectra of N-ZIF, N-ZIF/Co, and N-ZIF/CoPd-30.
 (D) High-resolution XPS spectra of N 1s of N-ZIF, N-ZIF/Co, and N-ZIF/CoPd-30.
 (E) High-resolution XPS spectra of Pd 3d of N-ZIF/CoPd-30.
 (F) High-resolution XPS spectra of Co 2p of N-ZIF, N-ZIF/Co, and N-ZIF/CoPd-30.

indicating that electron transfer from Co to Pd due to the difference in electronegativity ($\chi(\text{Co}) = 1.9$, $\chi(\text{Pd}) = 2.2$), implying that the Pd-Co heterojunction is a promising structure for electron enrichment at Pd sites.⁵⁶

Electrocatalytic activity

Firstly, the HER activity of as-synthesized electrocatalysts was evaluated by a standard three-electrode measurement system in 0.5 M H₂SO₄. Due to the HER performance of N-ZIF/Co was enhanced by varying the different content of Pd, and hence the impact of Pd content on the HER performance was first investigated. According to Figure S7A (see the supplemental information) and Figure 3A, the HER activity is enhanced with the increase of Pd content. In addition, the linear sweep voltammetry (LSV) curves exhibit that N-ZIF/CoPd-30 shows superior HER activity compared to N-ZIF/Co, N-ZIF and other control samples. In Figure 3B, it is notable that N-ZIF/CoPd-30 only demands an overpotential of 13 mV for generation of a current density of -10 mA cm^{-2} , much less than that of N-ZIF/Co (269 mV), N-ZIF (352 mV), and AC (937 mV). Additionally, the overpotential of N-ZIF/CoPd-30 (133 mV) is also lower than that of N-ZIF/Co (423 mV) at -100 mA cm^{-2} . The introduction of Pd reduces the overpotential of N-ZIF/Co at -10 mA cm^{-2} and -100 mA cm^{-2} by 256 mV and 290 mV, respectively. The Tafel slopes originating from the LSV curves in Figures 3A and S7A (see the supplemental information) were also studied to evaluate the hydrogen evolution kinetics of electrocatalysts. As shown in Figures 3C and S7B (see the supplemental information), the Tafel slope of N-ZIF/CoPd-30 (72 mV/decade) is much better than that of N-ZIF/Co (114 mV/decade), N-ZIF (153 mV/decade), N-ZIF/CoPd-1 (111 mV/decade), and N-ZIF/CoPd-10 (75 mV/decade), representing more efficient hydrogen evolution kinetics. Impressively, the acidic HER activity of N-ZIF/CoPd-30 can be compared to that of palladium-based HER catalysts and other platinum-like catalysts reported in the past few years as shown in Figures 3D and Tables S4 and S5 (see the supplemental information), implying that N-ZIF/CoPd-30 is a promising HER electrocatalyst.

Electrochemical impedance spectroscopy (EIS) and electrochemical active surface area (ECSA) were further performed to clarify the underlying root of the improved HER activity. EIS is used to evaluate the interfacial electron and proton transfer performance of electrocatalysts. The ideal Nyquist plot displays a semicircle in the high-frequency region, corresponding to the charge transfer resistance (R_{ct}) on the electrocatalytic reaction interface. The R_{ct} is calculated from the diameter of the semicircle in the high-frequency region. The smaller diameter represents the lower R_{ct} , indicating faster charge transfer. As shown in Figure 3E, N-ZIF/CoPd-30 possesses much lower charge transfer resistance than that of N-ZIF/Co, which reflects that N-ZIF/CoPd-30 has a faster charge transfer and higher charge transfer kinetics during the HER process. The reduced resistance reveals that the charge transfer process of catalyst is optimized.⁵⁷ Meanwhile, the charge transfer resistance of N-ZIF/CoPd decreases with the increase of Pd content as displayed in Figure S7C (see the supplemental information). Therefore, the introduction of Pd species into the N-ZIF/Co system can not only be effective in accelerating the reaction kinetics, but also reducing the charge transfer resistance, thus achieving a more ideal HER activity. Regarding ECSA, it is widely acknowledged that the linear relationship between the double layer capacitance (C_{dl}) and the ECSA of catalyst,⁵⁸ and CV measurements are conducted with different scan rates to obtain the C_{dl} .⁵⁹ The CV curves of different samples are exhibited in Figure S8 (see the supplemental information). Obviously, the higher C_{dl} value of N-ZIF/CoPd-30

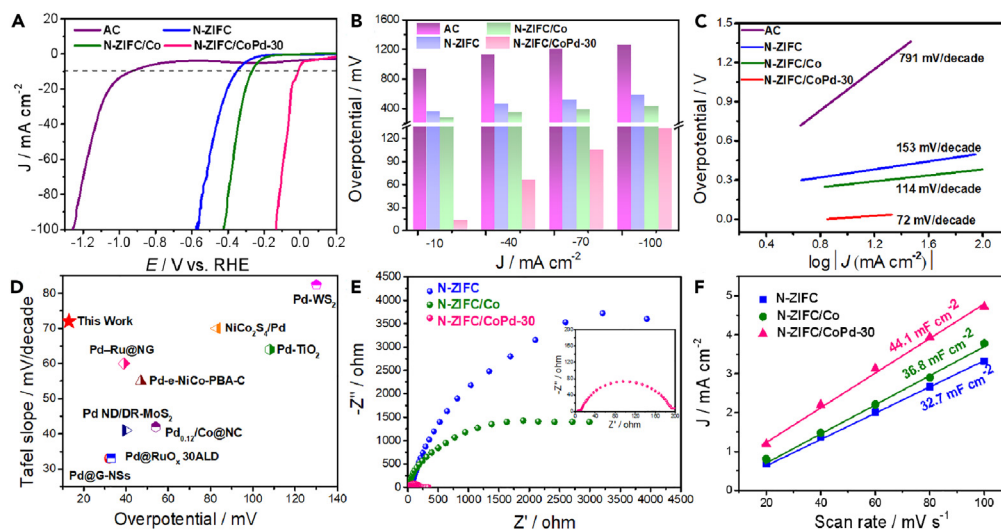


Figure 3. Electrochemical performance of the as-prepared catalysts in 0.5 M H₂SO₄

HER activity of AC, N-ZIFC, N-ZIFC/Co, and N-ZIFC/CoPd-30 in 0.5 M H₂SO₄.

(A) The LSV curves with iR-correction.

(B) The overpotential of different samples at current densities of -10 , -40 , -70 , and -100 mA cm⁻².

(C) Tafel slopes.

(D) Tafel slope and overpotential of N-ZIFC/CoPd-30 in comparison with other recently reported Pd-based HER electrocatalysts.

(E) Nyquist plots at -0.3 V (vs. Ag/AgCl).

(F) C_{dl} test of as-synthesized samples.

(44.1 mF cm⁻²) than that of N-ZIFC/Co (36.8 mF cm⁻²) and N-ZIFC (32.7 mF cm⁻²) manifests that more active sites are exposed by N-ZIFC/CoPd-30 for the electrocatalytic reaction (Figure 3F). The stability of catalyst is another essential aspect to assess the HER performance, except for the activity. As displayed in Figure S9 (see the supplemental information), N-ZIFC/CoPd-30 own well stability with negligible current decay at current density of about -30 mA cm⁻² for 60 h. The morphology and element content change of N-ZIFC/CoPd-30 after I-t test are further performed by SEM and element mapping. As shown in Figure S10 (see the supplemental information), the N-ZIFC/CoPd-30 catalyst still maintain the regular structure as before. In Figure S11 (see the supplemental information), besides C, N, Co, Pd, the existence of S and O originate from the residual sulfate ions in N-ZIFC/CoPd-30. Meanwhile, according to the Co, Pd content in the catalyst, the decline of HER performance is mainly due to the partial dissolution of Co during the stability test, thus breaking the Pd-Co heterojunction. These findings reveal that the N-ZIFC/CoPd-30 exhibit outstanding stability for HER, which is essential in general for electrocatalytic H₂ generation in acidic media.

Taking into account that three main methods for electrolyzing water (proton exchange membrane electrolysis, alkaline electrolysis, and microbial electrolysis) are applied in acidic, alkaline, and neutral environments, and the ideal electrocatalyst should retain substantial activity within a wide pH range for practical application. Since a series of N-ZIFC/CoPd samples exhibit excellent electrocatalytic HER activity in acidic environment, the N-ZIFC/CoPd catalysts were further evaluated in 0.1 M KOH to examine its pH universal activity. As presented in Figure S12A (see the supplemental information) and Figure 4A, the alkaline HER activities are enhanced with the increase of Pd content, and the N-ZIFC/CoPd-30 also performs the best electrocatalytic activity as before. As displayed in Figure 4B, it can be clearly observed that the N-ZIFC/CoPd-30 only requires an overpotential of 16 and 163 mV to provide a current density of -10 and -40 mA cm⁻², respectively. The Tafel slope of N-ZIFC/CoPd-30 is 98 mV/decade, better than that of N-ZIFC/Co (221 mV/decade), N-ZIFC (230 mV/decade), and other control samples as shown in Figures 4C and S12B (see the supplemental information). With such a low overpotential at -10 mA cm⁻² and Tafel slope, the N-ZIFC/CoPd-30 is expected to apply as a promising alkaline HER electrocatalyst. EIS and ECSA were further conducted, and the results are presented in the supplemental information. In Figure S12C (see the supplemental information), with the small charge transfer resistance, the N-ZIFC/CoPd-30 also achieves fast reaction kinetics and satisfactory alkaline HER activity, which broadly match the results obtained in acidic media. From Figure S13 (see the supplemental information), the N-ZIFC/CoPd-30 possess a greater C_{dl} value (29.2 mF cm⁻²) than that of N-ZIFC/Co (26.8 mF cm⁻²) and N-ZIFC (24.7 mF cm⁻²), implying that the N-ZIFC/CoPd-30 is able to expose a greater number of active sites, which is favorable for increasing the HER activity.

Though many materials exhibit excellent electrocatalytic HER activity under acidic or alkaline conditions, the HER performances of catalysts in the neutral pH environment are still unsatisfactory. Meanwhile, it is vital to generate H₂ from neutral solutions (such as sewage or river water) for environmental preservation and sustainable development. Therefore, the electrocatalytic activities of N-ZIFC/CoPd catalysts were further tested in 1.0 M PBS. Figures 4D–4F show the LSV curves, overpotential and Tafel plots of as-prepared samples. The overpotential of N-ZIFC/CoPd-30 at -10 mA cm⁻² is 162 mV, which is much lower than 314 and 267 mV of N-ZIFC and N-ZIFC/Co. Moreover, the overpotential of N-ZIFC/CoPd-30 is still less in comparison with N-ZIFC, N-ZIFC/Co, and AC at larger current density. The Tafel slopes of AC, N-ZIFC, N-ZIFC/Co, and N-ZIFC/CoPd-30 are 150, 143, 136, and 126 mV/decade, which also proves the favorable HER kinetics on N-ZIFC/CoPd-30. The Nyquist plots of

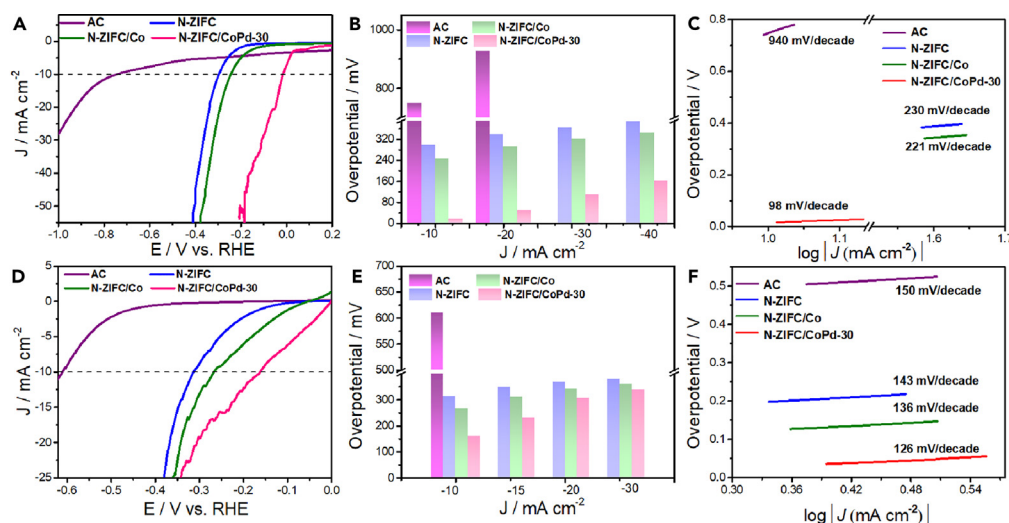


Figure 4. Electrocatalytic performance of the as-prepared catalysts in 0.1 M KOH and 1.0 M PBS

- (A) HER polarization curves with iR-correction.
 (B) The overpotential at current density of -10 , -20 , -30 , and -40 mA cm^{-2} .
 (C) Tafel plots of AC, N-ZIFC, N-ZIFC/Co, and N-ZIFC/CoPd-30 in 0.1 M KOH.
 (D) HER polarization curves with iR-correction.
 (E) The overpotential at current density of -10 , -15 , -20 , and -30 mA cm^{-2} .
 (F) Tafel plots of AC, N-ZIFC, N-ZIFC/Co, and N-ZIFC/CoPd-30 in 1.0 M PBS.

N-ZIFC, N-ZIFC/Co, and N-ZIFC/CoPd-30 in 1.0 M PBS are shown in Figure S14 (see the supplemental information). It can be clearly noticed that the N-ZIFC/CoPd-30 can achieve faster charge transfer at the interface of catalyst/electrolyte. ECSA was also carried out to determine the changes in the number of active sites among N-ZIFC, N-ZIFC/Co, and N-ZIFC/CoPd-30. From Figure S15 (see the supplemental information), the C_{dl} of N-ZIFC/CoPd-30 is 50.2 mF cm^{-2} , significantly greater than that of N-ZIFC/Co (38.6 mF cm^{-2}) and N-ZIFC (20.2 mF cm^{-2}). According to the aforementioned results, the high conductivity and abundant active sites are the key factors for N-ZIFC/CoPd-30 with outstanding HER kinetics in alkaline and neutral environments. Meanwhile, the stabilities of N-ZIFC/CoPd-30 in both alkaline and neutral media were evaluated as presented in Figure S16 (see the supplemental information). The current density has only a small attenuation in alkaline and neutral media, revealing its well stability for HER.

Mechanism analysis

To better understand the inherent nature of electrocatalytic H_2 evolution, DFT computations were performed by the VASP. The structural models of ZIFC, N-ZIFC, N-ZIFC/Pd, N-ZIFC/Co, and N-ZIFC/CoPd-30 can be depicted in Figures 5A, 5B, and S17 (see the supplemental information). The key point of calculation is to evaluate the electron transport between active site and substrate. As illustrated in Figure 5C, compared to the ZIFC structure, introducing nitrogen atoms break the electroneutrality of substrate, and cause the carbon π electrons to be activated. The result is that the carbon π electrons are easily transferred from in-plane to out-of-plane active sites, which can be confirmed by the Bader charge change of the adsorbed H (Δq). For clarity, the estimated Bader charge is the total of the Bader charges of one H atom, and negative values of the Bader charge change indicate the transfer of electrons from the catalyst surface to the adsorbed H, and the corresponding models are displayed in Figure S18 (see the supplemental information). The Δq values of ZIFC and N-ZIFC are in the order of $+0.08 e$ and $0 e$, indicating that the N-C polar bonds are successful in activating and inducing carbon π electrons transport. It is noteworthy that the Δq of $-0.73 e$ for Pd-Co site N-ZIFC/CoPd-30 is more negative than that of Co site N-ZIFC/Co and Pd site N-ZIFC/Pd, suggesting that the Pd-Co heterojunction play an important role in electron transport processes. Meanwhile, the differential charge density map also indicates that the charge density of Pd-Co heterojunction of N-ZIFC/CoPd-30 is redistributed in comparison with the Co site of N-ZIFC/Co and Pd site of N-ZIFC/Pd, revealing that the Co site can regulate the electronic structure of Pd site efficiently, which is consistent with the XPS results. Furthermore, the hydrogen adsorption free energy (ΔG_{H^*}) is also recognized as a critical parameter to evaluate the HER performance. The optimum HER electrocatalyst generally contains an ΔG_{H^*} value near zero, which speeds up hydrogen release while simultaneously enabling a quick proton/electron transfer.^{60,61} From Figures 5D and S19 (see the supplemental information), the ΔG_{H^*} of Pd-Co heterojunction of N-ZIFC/CoPd-30 is -0.16 eV , and much smaller than that of the Pd site of N-ZIFC/Pd (-0.34 eV), Co site of N-ZIFC/Co (-0.41 eV), ZIFC (1.44 eV), and N-ZIFC (0.94 eV), and can be compared to the most advanced Pt catalyst (-0.09 eV). These results demonstrate that Pd-Co heterojunction of N-ZIFC/CoPd-30 is a promising electrocatalyst for HER.

According to the theoretical calculations and experimental results, the activity-enhancing mechanism of electrocatalytic H_2 evolution over the Pd-Co heterojunction site of N-ZIFC/CoPd-30 was proposed (Figure 6). According to the XPS results, when Pd NPs loading on the surface

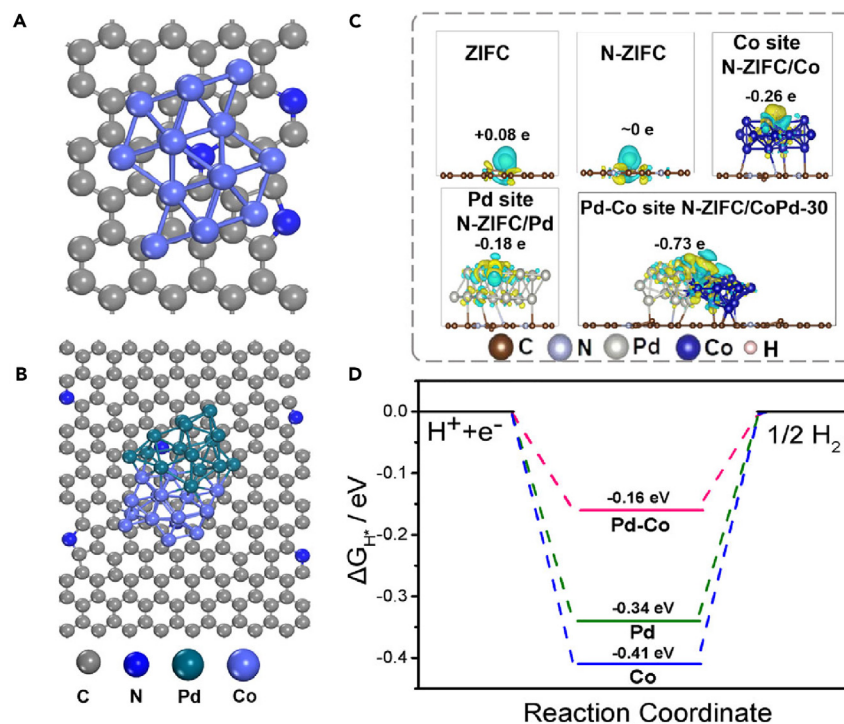


Figure 5. Theoretical interpretation

(A and B) Optimized structures of (A) N-ZIF/Co and (B) N-ZIF/CoPd-30.

(C) differential charge density map and Bader charge change (Δq) of H adsorbed on the basal-plane of ZIFC, N-ZIFC, Co site N-ZIF/Co, Pd site N-ZIF/Pd, Pd-Co site N-ZIF/CoPd-30, yellow and blue region indicate electron accumulation and depletion.

(D) Hydrogen adsorption free energy (ΔG_{H^+}) diagram of Co site N-ZIF/Co, Pd site N-ZIF/Pd, and Pd-Co site N-ZIF/CoPd-30.

of N-ZIF/Co, on the one hand, electron transfer from NC to Pd sites through the polar C-N bonds to induce activation of carbon π electrons. Meanwhile, Pd can form the Pd-Co heterojunction on the surface of N-ZIF/Co. Due to the difference in electronegativity between Co and Pd, electrons can also transfer from Co sites to Pd sites. Benefiting from the formation of C-N bonds and Co acting as “electron donors,” electron accumulation on Pd sites can lead to Pd species switching to electron-rich states. Based on the theoretical calculations results, the electron-rich Pd species possess a more ideal ΔG_{H^+} , which is critical for enhancing the wide pH range HER activity of catalyst.

Conclusions

In summary, the Pd deposition on the surface of Co NPs supported by N-doped carbon (N-ZIF/CoPd-30) has been successfully synthesized. The N-ZIF/CoPd-30 exhibits remarkable electrocatalytic HER activity with low overpotential (16, 162, and 13 mV@-10 mA cm⁻²) and small Tafel slopes (98, 126, and 72 mV/decade) in 0.1 M KOH, 1.0 M PBS, and 0.5 M H₂SO₄. Additionally, N-ZIF/CoPd-30 possesses excellent HER stability with no discernible performance degradation after 50 h in a wide pH range. The favorable activity and stability are attributed to the following factors based on experimental and DFT results. The formation of C-N polar bonds and Pd-Co heterojunction can enhance the strong interaction between N-ZIF/Co substrate and Pd site, and promote Pd transforming into the electron-rich state, which is favorable to accelerate the hydrogen absorption/desorption, as well as thus boost the electrocatalytic HER performance. This study provides a valuable inspiration to construct heterojunction functional catalysts in the promising practical application for electrocatalytic H₂ production.

Limitations of the study

Although the electron-rich Pd site in N-ZIF/CoPd-30 was beneficial to HER from theoretical calculations, the experimental proof for this point is lacking. Future research will focus on the identification of the active site by employing more experimental characterization to make the theoretical results more convincing.

STAR★METHODS

Detailed methods are provided in the online version of this paper and include the following:

- KEY RESOURCES TABLE

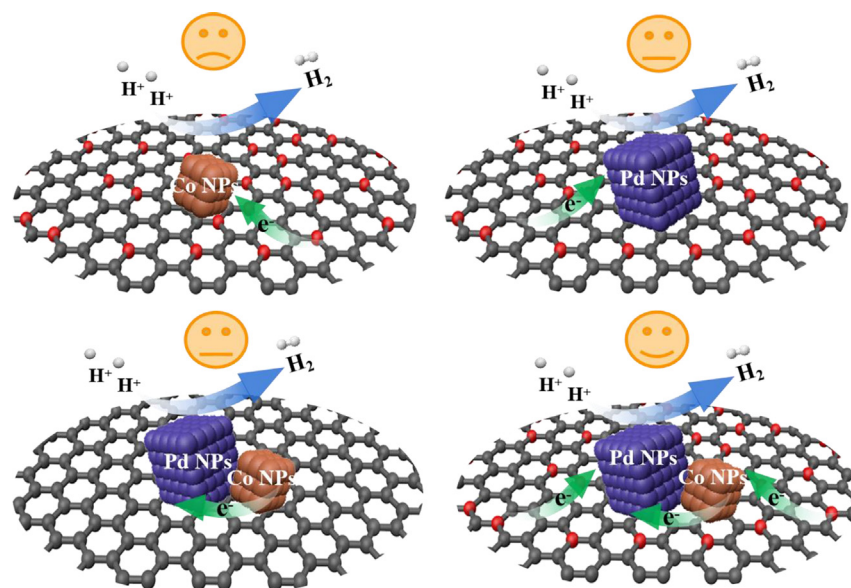


Figure 6. Schematic illustration for electrocatalytic H₂ evolution over N-ZIFC/CoPd-30

● **RESOURCE AVAILABILITY**

- Lead contact
- Materials availability
- Data and code availability

● **METHOD DETAILS**

- Preparation of N-ZIFC/Co samples
- Preparation of N-ZIFC/CoPd samples
- Preparation of N-ZIFC samples
- Characterizations of electrocatalysts
- Electrochemical measurements
- Calculation details

SUPPLEMENTAL INFORMATION

Supplemental information can be found online at <https://doi.org/10.1016/j.isci.2024.109620>.

ACKNOWLEDGMENTS

This work was supported by Jiangxi Provincial Natural Science Foundation (20232BAB204088), the Self-deployed Projects of Ganjiang Innovation Academy, Chinese Academy of Sciences (E055A001), the Key Research Program of the Chinese Academy of Sciences (ZDRW-CN-2021-3), the Double Thousand Plan of Jiangxi Province (jxsq2020105012), and the Research Projects of Ganjiang Innovation Academy, Chinese Academy of Sciences (E055ZA01).

AUTHOR CONTRIBUTIONS

C.Z.: conceptualization, investigation, formal analysis, data curation, and writing – original draft; S.S.: resources; X.Z.: investigation and data curation; Y.S.: investigation and validation; G.P.: methodology, software, and formal analysis; W.Y.: supervision, funding acquisition, resources, and writing – review & editing.

DECLARATION OF INTERESTS

The authors declare no competing interests.

Received: November 20, 2023

Revised: February 4, 2024

Accepted: March 26, 2024

Published: March 28, 2024

REFERENCES

- Chi, J., and Yu, H. (2018). Water electrolysis based on renewable energy for hydrogen production. *Chin. J. Catal.* 39, 390–394. [https://doi.org/10.1016/S1872-2067\(17\)62949-8](https://doi.org/10.1016/S1872-2067(17)62949-8).
- Li, P., Wang, Y., Du, X., and Zhang, X. (2023). Controlled synthesis of ACo_2O_4 (A = Fe, Cu, Zn, Ni) as an environmentally friendly electrocatalyst for urea electrolysis. *Dalton Trans.* 52, 10499–10506. <https://doi.org/10.1039/D3DT01845H>.
- Wang, H., Yang, P., Sun, X., Xiao, W., Wang, X., Tian, M., Xu, G., Li, Z., Zhang, Y., Liu, F., et al. (2023). Co-Ru alloy nanoparticles decorated onto two-dimensional nitrogen doped carbon nanosheets toward hydrogen/oxygen evolution reaction and oxygen reduction reaction. *J. Energy Chem.* 87, 286–294. <https://doi.org/10.1016/j.jechem.2023.08.039>.
- Lu, H., Tournet, J., Dastafkan, K., Liu, Y., Ng, Y.H., Karuturi, S.K., Zhao, C., and Yin, Z. (2021). Noble-Metal-Free Multicomponent Nanointegration for Sustainable Energy Conversion. *Chem. Rev.* 121, 10271–10366. <https://doi.org/10.1021/acs.chemrev.0c01328>.
- Zhu, J., Hu, L., Zhao, P., Lee, L.Y.S., and Wong, K.-Y. (2020). Recent Advances in Electrocatalytic Hydrogen Evolution Using Nanoparticles. *Chem. Rev.* 120, 851–918. <https://doi.org/10.1021/acs.chemrev.9b00248>.
- Wang, C., Wang, Q., Du, X., and Zhang, X. (2023). Controlled synthesis of M doped Ni_5S_2 (M = Co, Ce and Cr) as a robust electrocatalyst for urea electrolysis. *Dalton Trans.* 52, 13161–13168. <https://doi.org/10.1039/D3DT02586A>.
- Liu, G., Xu, Y., Yang, T., and Jiang, L. (2023). Recent advances in electrocatalysts for seawater splitting. *Nano Materials Sci.* 5, 101–116. <https://doi.org/10.1016/j.nanoms.2020.12.003>.
- Xing, Y., Li, D., Li, L., Tong, H., Jiang, D., and Shi, W. (2021). Accelerating water dissociation kinetic in Co_9S_8 electrocatalyst by mn/N Co-doping toward efficient alkaline hydrogen evolution. *Int. J. Hydrogen Energy* 46, 7989–8001. <https://doi.org/10.1016/j.ijhydene.2020.12.037>.
- Zhang, Z., Chen, K., Zhao, Q., Huang, M., and Ouyang, X. (2021). Electrocatalytic and photocatalytic performance of noble metal doped monolayer MoS_2 in the hydrogen evolution reaction: A first principles study. *Nano Materials Sci.* 3, 89–94. <https://doi.org/10.1016/j.nanoms.2020.05.001>.
- Tang, R., Yang, Y., Zhou, Y., and Yu, X.Y. (2023). Rational Design of Heterostructured Ru Cluster-Based Catalyst for pH Universal Hydrogen Evolution Reaction and High-Performance Zn-H₂O Battery. *Adv. Funct. Mater.* 34, 2301925. <https://doi.org/10.1002/adfm.202301925>.
- Zhang, S.L., Lu, X.F., Wu, Z.P., Luan, D., and Lou, X.W.D. (2021). Engineering Platinum–Cobalt Nano-alloys in Porous Nitrogen-Doped Carbon Nanotubes for Highly Efficient Electrocatalytic Hydrogen Evolution. *Angew. Chem. Int. Ed. Engl.* 60, 19068–19073. <https://doi.org/10.1002/anie.202106547>.
- Chen, Z., Li, Q., Xiang, H., Wang, Y., Yang, P., Dai, C., Zhang, H., Xiao, W., Wu, Z., and Wang, L. (2023). Hierarchical porous NiFe-P@NC as an efficient electrocatalyst for alkaline hydrogen production and seawater electrolysis at high current density. *Inorg. Chem. Front.* 10, 1493–1500. <https://doi.org/10.1039/D2QI02703H>.
- Gandu, B., Rozenfeld, S., Ouaknin Hirsch, L., Schechter, A., and Cahan, R. (2020). Immobilization of bacterial cells on carbon-cloth anode using alginate for hydrogen generation in a microbial electrolysis cell. *J. Power Sources* 455, 227986. <https://doi.org/10.1016/j.jpowsour.2020.227986>.
- Xie, X., Song, M., Wang, L., Engelhard, M.H., Luo, L., Miller, A., Zhang, Y., Du, L., Pan, H., Nie, Z., et al. (2019). Electrocatalytic Hydrogen Evolution in Neutral pH Solutions: Dual-Phase Synergy. *ACS Catal.* 9, 8712–8718. <https://doi.org/10.1021/acscatal.9b02609>.
- Hu, C., Zhang, L., and Gong, J. (2019). Recent progress made in the mechanism comprehension and design of electrocatalysts for alkaline water splitting. *Energy Environ. Sci.* 12, 2620–2645. <https://doi.org/10.1039/C9EE01202H>.
- Wu, Z., Zhao, Y., Xiao, W., Fu, Y., Jia, B., Ma, T., and Wang, L. (2022). Metallic-Bonded Pt–Co for Atomically Dispersed Pt in the Co_4N Matrix as an Efficient Electrocatalyst for Hydrogen Generation. *ACS Nano* 16, 18038–18047. <https://doi.org/10.1021/acsnano.2c04090>.
- Wu, Z., Yang, P., Li, Q., Xiao, W., Li, Z., Xu, G., Liu, F., Jia, B., Ma, T., Feng, S., and Wang, L. (2023). Microwave Synthesis of Pt Clusters on Black TiO_2 with Abundant Oxygen Vacancies for Efficient Acidic Electrocatalytic Hydrogen Evolution. *Angew. Chem. Int. Ed. Engl.* 62, e202300406. <https://doi.org/10.1002/anie.202300406>.
- Zhao, Y., Gao, Y., Chen, Z., Li, Z., Ma, T., Wu, Z., and Wang, L. (2021). Triflate Pt coupled with NiFe hydroxide synthesized via corrosion engineering to boost the cleavage of water molecule for alkaline water-splitting. *Appl. Catal. B Environ.* 297, 120395. <https://doi.org/10.1016/j.apcatb.2021.120395>.
- Wang, Y., Su, H., He, Y., Li, L., Zhu, S., Shen, H., Xie, P., Fu, X., Zhou, G., Feng, C., et al. (2020). Advanced Electrocatalysts with Single-Metal-Atom Active Sites. *Chem. Rev.* 120, 12217–12314. <https://doi.org/10.1021/acs.chemrev.0c00594>.
- Ma, J., Wang, J., Liu, J., Li, X., Sun, Y., and Li, R. (2022). Electron-rich ruthenium encapsulated in nitrogen-doped carbon for efficient hydrogen evolution reaction over the whole pH. *J. Colloid Interface Sci.* 620, 242–252. <https://doi.org/10.1016/j.jcis.2022.03.149>.
- Li, Q., Wang, X., Xie, Z., Peng, X., Guo, L., Yu, X., Yang, X., Lu, Z., Zhang, X., and Li, L. (2022). Polar bonds induced strong Pd-support electronic interaction drives remarkably enhanced oxygen reduction activity and stability. *Appl. Catal. B Environ.* 305, 121020. <https://doi.org/10.1016/j.apcatb.2021.121020>.
- Sun, Y.-B., Ni, M., Chi, C., Yang, D.-R., Chen, X.-L., Qi, Q., Li, J., and Xia, X.-H. (2023). Plasmon driven super-high HER activity of electronic structure and lattice strain engineered single atomic layer Pd@Au nanorods. *Chem. Eng. J.* 467, 143387. <https://doi.org/10.1016/j.cej.2023.143387>.
- Li, G., Khim, S., Chang, C.S., Fu, C., Nandi, N., Li, F., Yang, Q., Blake, G.R., Parkin, S., Auffermann, G., et al. (2019). In Situ Modification of a Delafossite-Type PdCoO_2 Bulk Single Crystal for Reversible Hydrogen Sorption and Fast Hydrogen Evolution. *ACS Energy Lett.* 4, 2185–2191. <https://doi.org/10.1021/acsenergylett.9b01527>.
- Chen, H., Yuan, M., Zhai, C., Tan, L., Cong, N., Han, J., Fang, H., Zhou, X., Ren, Z., and Zhu, Y. (2020). Nano PdFe Alloy Assembled Film as a Highly Efficient Electrocatalyst toward Hydrogen Evolution in Both Acid and Alkaline Solutions. *ACS Appl. Energy Mater.* 3, 8969–8977. <https://doi.org/10.1021/acsaem.0c01410>.
- Kaya, D., Isik, H.H., Isik, I.B., Sigircik, G., Tuken, T., Karadag, F., and Ekicibil, A. (2023). Electrocatalytic hydrogen evolution on metallic and bimetallic Pd–Co alloy nanoparticles. *Int. J. Hydrogen Energy* 48, 14633–14641. <https://doi.org/10.1016/j.ijhydene.2023.01.049>.
- Flores Espinosa, M.M., Cheng, T., Xu, M., Abatemarco, L., Choi, C., Pan, X., Goddard, W.A., III, Zhao, Z., and Huang, Y. (2020). Compressed Intermetallic PdCu for Enhanced Electrocatalysis. *ACS Energy Lett.* 5, 3672–3680. <https://doi.org/10.1021/acsenergylett.0c01959>.
- Liu, X.L., Jiang, Y.C., Huang, J.T., Zhong, W., He, B., Jin, P.J., and Chen, Y. (2023). Bifunctional PdPt bimetalloenes for formate oxidation-boosted water electrolysis. *Carbon Energy* 5, e367. <https://doi.org/10.1002/cey2.367>.
- Liu, S., Zhang, H., Yu, H., Deng, K., Wang, Z., Xu, Y., Wang, L., and Wang, H. (2023). Defect-Rich PdIr Bimetallic Nanoribbons with Interatomic Charge Localization for Isopropanol-Assisted Seawater Splitting. *Small* 19, 2300388. <https://doi.org/10.1002/sml.202300388>.
- Liu, S., Zhang, H., Yu, H., Deng, K., Wang, Z., Xu, Y., Wang, L., and Wang, H. (2023). Tailored design of PdRh bimetallic nanoribbons by solvent-induced strategy for efficient alkaline hydrogen evolution. *Appl. Catal. B Environ.* 336, 122948. <https://doi.org/10.1016/j.apcatb.2023.122948>.
- Ge, Y., Ge, J., Huang, B., Wang, X., Liu, G., Shan, X.-H., Ma, L., Chen, B., Liu, G., Du, S., et al. (2023). Synthesis of amorphous Pd-based nanocatalysts for efficient alcoholysis of styrene oxide and electrochemical hydrogen evolution. *Nano Res.* 16, 4650–4655. <https://doi.org/10.1007/s12274-022-5101-0>.
- Ding, J., Jiang, X., Wang, C., Zhu, Z., Xu, C., Zhou, Y., Wang, X., Liu, Q., Liu, Z., Tang, Y., et al. (2023). Epitaxial growth triggered core-shell Pd@RuP nanorods for high-efficiency electrocatalytic hydrogen evolution. *J. Energy Chem.* 86, 510–517. <https://doi.org/10.1016/j.jechem.2023.07.035>.
- Chalgin, A., Chen, W., Xiang, Q., Wu, Y., Li, F., Shi, F., Song, C., Tao, P., Shang, W., and Wu, J. (2020). Manipulation of Electron Transfer between Pd and TiO_2 for Improved Electrocatalytic Hydrogen Evolution Reaction Performance. *ACS Appl. Mater. Interfaces* 12, 27037–27044. <https://doi.org/10.1021/acsaami.0c03742>.
- Li, J., Cheng, Y., Zhang, J., Fu, J., Yan, W., and Xu, Q. (2019). Confining Pd Nanoparticles and Atomically Dispersed Pd into Defective MoO_3 Nanosheet for Enhancing Electro- and Photocatalytic Hydrogen Evolution Performances. *ACS Appl. Mater. Interfaces* 11, 27798–27804. <https://doi.org/10.1021/acsaami.9b07469>.

34. Zheng, B., Gao, X., Li, M., Deng, T., Huang, Z., Zhou, H., Li, D., Liu, M., Qiu, X., Chen, W., and Chen, W. (2019). Strong Electron Coupling from the Sub-Nanometer Pd Clusters Confined in Porous Ceria Nanorods for Highly Efficient Electrochemical Hydrogen Evolution Reaction. *Polymers* 11, 966–973. <https://doi.org/10.1021/acsaem.8b01783>.
35. Zhang, Y., Chen, L., Gui, Y., and Liu, L. (2022). Catalytic transfer hydrogenation of nitrobenzene over Ti₃C₂/Pd nanohybrids boosted by electronic modification and hydrogen evolution inhibition. *Appl. Surf. Sci.* 592, 153334. <https://doi.org/10.1016/j.apsusc.2022.153334>.
36. Wang, D., Yang, H., Tian, S., Liu, G., Wang, Y., Sun, X., Wang, Z., Hou, J., Ma, F., and Peng, S. (2023). High dispersion Pd nanoclusters modified sulfur-rich vacancies ZnIn₂S₄ for high-performance hydrogen evolution. *Appl. Surf. Sci.* 638, 157926. <https://doi.org/10.1016/j.apsusc.2023.157926>.
37. Qi, K., Yu, S., Wang, Q., Zhang, W., Fan, J., Zheng, W., and Cui, X. (2016). Decoration of the inert basal plane of defect-rich MoS₂ with Pd atoms for achieving Pt-similar HER activity. *J. Mater. Chem. A Mater.* 4, 4025–4031. <https://doi.org/10.1039/C5TA10337A>.
38. Zhao, X., Li, X., Xiao, D., Gong, M., An, L., Gao, P., Yang, J., and Wang, D. (2021). Isolated Pd atom anchoring endows cobalt diselenides with regulated water-reduction kinetics for alkaline hydrogen evolution. *Appl. Catal. B Environ.* 295, 120280. <https://doi.org/10.1016/j.apcatb.2021.120280>.
39. Karuppasamy, L., Gurusamy, L., Anandan, S., Liu, C.-H., and Wu, J.J. (2021). Graphene nanosheets supported high-defective Pd nanocrystals as an efficient electrocatalyst for hydrogen evolution reaction. *Chem. Eng. J.* 425, 131526. <https://doi.org/10.1016/j.cej.2021.131526>.
40. Guo, K., Rowland, L.J., Isherwood, L.H., Glodan, G., and Baidak, A. (2020). Photon-induced synthesis of ultrathin metal nanoparticles on graphene as electrocatalysts: impact of functionalization and doping. *J. Mater. Chem. A Mater.* 8, 714–723. <https://doi.org/10.1039/C9TA10518B>.
41. Gao, H., Zang, J., Liu, X., Wang, Y., Tian, P., Zhou, S., Song, S., Chen, P., and Li, W. (2019). Ruthenium and cobalt bimetal encapsulated in nitrogen-doped carbon material derived of ZIF-67 as enhanced hydrogen evolution electrocatalyst. *Appl. Surf. Sci.* 494, 101–110. <https://doi.org/10.1016/j.apsusc.2019.07.181>.
42. Zhang, M., Dai, Q., Zheng, H., Chen, M., and Dai, L. (2018). Novel MOF-Derived Co@N-C Bifunctional Catalysts for Highly Efficient Zn-Air Batteries and Water Splitting. *Adv. Mater.* 30, 201705431. <https://doi.org/10.1002/adma.201705431>.
43. Mo, Q., Chen, N., Deng, M., Yang, L., and Gao, Q. (2017). Metallic Cobalt@Nitrogen-Doped Carbon Nanocomposites: Carbon-Shell Regulation toward Efficient Bi-Functional Electrocatalysis. *ACS Appl. Mater. Interfaces* 9, 37721–37730. <https://doi.org/10.1021/acsaami.7b10853>.
44. Song, Y., Xie, W., Shao, M., and Duan, X. (2023). Integrated electrocatalysts derived from metal organic frameworks for gas-involved reactions. *Nano Materials Sci.* 5, 161–176. <https://doi.org/10.1016/j.nanoms.2022.01.003>.
45. Yang, H., Tang, Z., Wang, K., Wu, W., Chen, Y., Ding, Z., Liu, Z., and Chen, S. (2018). Co@Pd core-shell nanoparticles embedded in nitrogen-doped porous carbon as dual functional electrocatalysts for both oxygen reduction and hydrogen evolution reactions. *J. Colloid Interface Sci.* 528, 18–26. <https://doi.org/10.1016/j.jcis.2018.05.063>.
46. Liu, H., Liu, C., Zong, X., Wang, Y., Hu, Z., and Zhang, Z. (2023). Highly uniform Pd nanoparticles supported on Co-metal organic frameworks-derived carbon as HER electrocatalysts. *Int. J. Hydrogen Energy* 48, 31152–31160. <https://doi.org/10.1016/j.ijhydene.2023.04.150>.
47. Zong, Z., Xu, K., Li, D., Tang, Z., He, W., Liu, Z., Wang, X., and Tian, Y. (2018). Peptide templated Au@Pd core-shell structures as efficient bi-functional electrocatalysts for both oxygen reduction and hydrogen evolution reactions. *J. Catal.* 361, 168–176. <https://doi.org/10.1016/j.jcat.2018.02.020>.
48. Zhang, Y.-L., Shen, W.-J., Kuang, W.-T., Guo, S., Li, Y.-J., and Wang, Z.-H. (2017). Serrated Au/Pd Core/Shell Nanowires with Jagged Edges for Boosting Liquid Fuel Electrooxidation. *ChemSusChem* 10, 2375–2379. <https://doi.org/10.1002/cssc.201700602>.
49. Liu, M., Zhang, M., Zhang, P., Xing, Z., Jiang, B., Yu, Y., Cai, Z., Li, J., and Zou, J. (2020). ZIF-67-Derived Dodecahedral Co@N-Doped Graphitized Carbon Protected by a Porous FeS₂ Thin-Layer as an Efficient Catalyst to Promote the Oxygen Reduction Reaction. *ACS Sustain. Chem. Eng.* 8, 4194–4206. <https://doi.org/10.1021/acssuschemeng.9b07276>.
50. Lee, S.H., Kim, J., Chung, D.Y., Yoo, J.M., Lee, H.S., Kim, M.J., Mun, B.S., Kwon, S.G., Sung, Y.-E., and Hyeon, T. (2019). Design Principle of Fe–N–C Electrocatalysts: How to Optimize Multimodal Porous Structures? *J. Am. Chem. Soc.* 141, 2035–2045. <https://doi.org/10.1021/jacs.8b11129>.
51. Liu, S., Wang, Z., Guo, X., Hu, Z., Wang, H., and Zhang, G. (2021). N-Doped Porous Carbon-Anchored Pd Nanoparticles: A Highly Efficient Catalyst for Fe(II)EDTA-NO Reduction. *J. Phys. Chem. C* 125, 17068–17077. <https://doi.org/10.1021/acs.jpcc.1c04736>.
52. Liu, Q., Peng, Y., Li, Q., He, T., Morris, D., Nichols, F., Mercado, R., Zhang, P., and Chen, S. (2020). Atomic Dispersion and Surface Enrichment of Palladium in Nitrogen-Doped Porous Carbon Cages Lead to High-Performance Electrocatalytic Reduction of Oxygen. *ACS Appl. Mater. Interfaces* 12, 17641–17650. <https://doi.org/10.1021/acsaami.0c03415>.
53. Ding, X., Chen, Y., Nan, J., Dai, H., Wang, Y., Bai, G., and Qiu, W. (2022). Ultrasmall Palladium Nanoparticles Anchored on N-Doped Nestlike Carbon Nanosheets for Selective Hydrogenation of Quinolines. *ACS Sustain. Chem. Eng.* 10, 14011–14023. <https://doi.org/10.1021/acssuschemeng.2c04585>.
54. Chaparro-Garnica, J., Navlani-García, M., Salinas-Torres, D., Morallón, E., and Cazorla-Amorós, D. (2020). Highly Stable N-Doped Carbon-Supported Pd-Based Catalysts Prepared from Biomass Waste for H₂ Production from Formic Acid. *ACS Sustain. Chem. Eng.* 8, 15030–15043. <https://doi.org/10.1021/acssuschemeng.0c05906>.
55. Shang, Y., Liu, C., Zhang, Z., Wang, S., Zhao, C., Yin, X., Zhang, P., Liu, D., and Gui, J. (2020). Insights into the Synergistic Effect in Pd Immobilized to MOF-Derived Co-CoO_x@N-Doped Carbon for Efficient Selective Hydrogenolysis of 5-Hydroxymethylfurfural. *Ind. Eng. Chem. Res.* 59, 6532–6542. <https://doi.org/10.1021/acs.iecr.9b07099>.
56. Zhao, D., Li, Z., Yu, X., Zhou, W., Wu, Q., Luo, Y., Wang, N., Liu, A., Li, L., and Chen, S. (2022). Ru decorated Co nanoparticles supported by N-doped carbon sheet implements Pt-like hydrogen evolution performance in wide pH range. *Chem. Eng. J.* 450, 138254. <https://doi.org/10.1016/j.cej.2022.138254>.
57. Wan, C., Jin, J., Wei, X., Chen, S., Zhang, Y., Zhu, T., and Qu, H. (2022). Inducing the SnO₂-based electron transport layer into NiFe LDH/NF as efficient catalyst for OER and methanol oxidation reaction. *J. Mater. Sci. Technol.* 124, 102–108. <https://doi.org/10.1016/j.jmst.2022.01.022>.
58. Li, C., Jang, H., Kim, M.G., Hou, L., Liu, X., and Cho, J. (2022). Ru-incorporated oxygen-vacancy-enriched MoO₂ electrocatalysts for hydrogen evolution reaction. *Appl. Catal. B Environ.* 307, 121204. <https://doi.org/10.1016/j.apcatb.2022.121204>.
59. Sun, R.-M., Zhang, L., Feng, J.-J., Fang, K.-M., and Wang, A.-J. (2022). In situ produced Co₉S₈ nanoclusters/Co/Mn-S, N multi-doped 3D porous carbon derived from eriochrome black T as an effective bifunctional oxygen electrocatalyst for rechargeable Zn-air batteries. *J. Colloid Interface Sci.* 608, 2100–2110. <https://doi.org/10.1016/j.jcis.2021.10.144>.
60. Zhou, S., Chen, X., Li, T., Wei, Y., Sun, R., Han, S., and Jiang, J. (2024). Heterogeneous interface engineering of cationic vacancy defects layered double hydroxides and molybdenum-nickel-based selenium compounds to facilitate overall water splitting. *Fuel* 357, 129732. <https://doi.org/10.1016/j.fuel.2023.129732>.
61. Zhou, N., Zhang, R., Wang, R., and Li, Y. (2023). Preparation of PtNiCo alloy/nitrogen-doped porous carbon composites and their electrocatalytic properties. *Chem. Eng. J.* 474, 146010. <https://doi.org/10.1016/j.cej.2023.146010>.

STAR★METHODS

KEY RESOURCES TABLE

REAGENT or RESOURCE	SOURCE	IDENTIFIER
Chemicals, peptides, and recombinant proteins		
2-methylimidazole (C ₄ H ₆ N ₂ , 98%)	Macklin	CAS: 693-98-1
cobalt nitrate hexahydrate (Co(NO ₃) ₂ ·6H ₂ O, 99%)	Macklin	CAS: 10026-22-9
Palladium chloride (PdCl ₂ , 99.999%)	Aladdin	CAS: 7647-10-1
Methanol (CH ₃ OH, 99.5%)	Xilong Scientific Co., Ltd	CAS: 67-56-1
Argon (Ar, 99.999%)	Yingde City Xizhou Gas Co., Ltd	
5 vol % H ₂ (Ar balance)	Yingde City Xizhou Gas Co., Ltd	

RESOURCE AVAILABILITY

Lead contact

Further information and requests for resources and materials should be directed to and will be fulfilled by the lead contact, Dr. Wenjing Yuan (wjyuan@gia.cas.cn).

Materials availability

This study did not generate new unique reagents.

Data and code availability

- Data reported in this paper will be shared by the [lead contact](#) upon request.
- This paper does not report original code.
- Any additional information required to reanalyze the data reported in this paper is available from the [lead contact](#) upon request.

METHOD DETAILS

Preparation of N-ZIFC/Co samples

In a typical synthesis, 300 mL of methanol was used to dissolve 11.64 g of Co(NO₃)₂·6H₂O, and the formed solution was marked as solution A. As solution B, 300 mL of methanol was employed to dissolve 12.32 g of C₄H₆N₂. The purple turbid solution was generated by immediately combining solution B with solution A, and then allowed to stand for 24 h at room temperature. Filter cake was gathered, and washed with methanol 3 times, and then heated in the oven at 60°C for 12 h to obtain ZIF-67 powder. The dried ZIF-67 was put in a tube furnace, and carbonized within an Ar atmosphere at 450°C and 900°C for 1 h, respectively, to obtain nitrogen-doped porous ZIF carbon loaded with Co NPs, which were labeled as N-ZIFC/Co.

Preparation of N-ZIFC/CoPd samples

The 1, 10 and 30 mL of PdCl₂ solutions (2 mg/mL) were added to the centrifuge tube containing 250 mg N-ZIFC/Co, respectively. After a period of time, it was dried in the oven at 80°C for 3 days. Finally, the dried precursor was heated in 5 vol % H₂ (Ar balance) at 400°C for 1 h, and the Pd²⁺ adsorbed on the surface of N-ZIFC/Co was reduced to Pd NPs, and obtained final product, and marked as N-ZIFC/CoPd-1, N-ZIFC/CoPd-10 and N-ZIFC/CoPd-30.

Preparation of N-ZIFC samples

The control sample (N-ZIFC) was also prepared by annealing the dried ZIF-67 powder in Ar atmosphere at 450°C and 900°C for 1 h in turn, and then the obtained N-ZIFC/Co was etched with HCl to dissolve the Co NPs on its surface.

Characterizations of electrocatalysts

The phase composition was confirmed by a Bruker D8 Advance X-ray diffractometer. The morphology and microstructure of samples were characterized by an FEI Scios 2 HiVac scanning electron microscope (SEM) and a JEOL2100F TEM. XPS was obtained on an EscaLab Xi+ instrument. The Brunauer-Emmett-Teller (BET) surface area was measured on a Micromeritics ASAP 2460 instrument.

Electrochemical measurements

CHI 660E electrochemical workstation (Shanghai Chenhua, China) combined with a typical three-electrode system was used to evaluate the HER performance of samples. Firstly, 30 mg of the sample was dispersed in ethanol (3.0 mL) to form ink (10 mg mL^{-1}), and then the glassy carbon electrode surface was dripped with $10 \mu\text{L}$ of catalyst ink. Subsequently, a suitable amount of Nafion solution (0.05 wt %) was used to adhere the catalyst, and thoroughly dried at room temperature. The mass loading of as-prepared sample is 1.41 mg cm^{-2} for HER, and the contents of Pd on the electrode for N-ZIFC/CoPd-1, N-ZIFC/CoPd-10 and N-ZIFC/CoPd-30 are $0.0090 \text{ mg cm}^{-2}$, $0.0455 \text{ mg cm}^{-2}$ and 0.15 mg cm^{-2} , respectively. In acidic, alkaline, and neutral media, a glassy carbon electrode, an Ag/AgCl electrode and a graphite rod were used as working electrode, reference electrode and counter electrode, respectively. The sample loaded on carbon paper ($1 \times 1 \text{ cm}$) (loading: 0.5 mg cm^{-2}) was used to evaluate the stability of electrocatalysts in $0.5 \text{ M H}_2\text{SO}_4$, 0.1 M KOH , and 1.0 M PBS . All potentials were compensated for iR and converted to the reversible hydrogen electrode (RHE) scale according to Equation 1. LSVs were studied at a scan rate of 5 mV s^{-1} with 100% iR -corrected. EIS was performed at -0.3 V (vs. Ag/AgCl) in H_2SO_4 , -1.1 V (vs. Ag/AgCl) in KOH, and -0.75 V (vs. Ag/AgCl) in PBS from 10^6 to 0.01 Hz . The CV curves were measured in the non-Faradaic region of potential from 0.047 V to 0.147 V (versus RHE) in $0.5 \text{ M H}_2\text{SO}_4$, from 0.167 V to 0.267 V (versus RHE) in 0.1 M KOH , and from 0.111 V to 0.211 V (versus RHE) in 1.0 M PBS from 20 mV s^{-1} to 100 mV s^{-1} to estimate the double layer capacitance (C_{dl}) and electrochemically active surface area (ECSA).

$$E_{\text{RHE}} = E_{\text{Ag/AgCl}} + 0.197\text{V} + 0.0592\text{pH} \quad (\text{Equation 1})$$

Calculation details

The Vienna Ab initio Simulation Package (VASP) was applied to perform the DFT calculations using an all-electron plane-wave basis set with a 520 eV energy cutoff and a spin-polarized GGA PBE functional. The conjugate gradient algorithm was implemented for the optimization. The projector augmented wave method and a $(3 \times 3 \times 1)$ Monkhorst-Pack mesh were adopted for the Brillouin-zone integrations to be sampled, and the convergence thresholds for total energy and force on each atom were set at $1 \times 10^{-5} \text{ eV}$ and 0.02 eV/\AA , respectively. The change of adsorption energy (ΔE_{ads}) and free energy (ΔG) for adsorptions were calculated based on the Equations 2 and 3.

$$\Delta E_{\text{ads}} = E_{\text{total}} - E_{\text{sur}} - E_{\text{mol}} \quad (\text{Equation 2})$$

$$\Delta G = E_{\text{total}} - E_{\text{sur}} - E_{\text{mol}} + \Delta E_{\text{ZPE}} - T\Delta S \quad (\text{Equation 3})$$

E_{total} , E_{sur} , E_{mol} , ΔE_{ZPE} and ΔS represent total energy for the adsorption state, energy of pure surface, energy of adsorption molecule, zero-point energy and entropy change in turn. Due to the small value of the vibrational entropy of H^* in the adsorbed state, the entropy of adsorption of $1/2 \text{ H}_2$ is $S_{\text{H}} \approx -0.5S_{0\text{H}_2}$, where the $S_{0\text{H}_2}$ stands for the entropy of H_2 in the gas phase under the standard conditions. Based on this, the overall corrections were represented by the Equation 4, and the E_{H_2} is the energy of H_2 in gas phase.

$$\Delta G_{\text{H}^*} = E_{\text{total}} - E_{\text{sur}} - \frac{1}{2}E_{\text{H}_2} + 0.24 \text{ eV} \quad (\text{Equation 4})$$